



# Particle Image Velocimetry Measurements in Accelerated, Transonic Wake Flows

Judith Richter<sup>1</sup> · Charalampos Alexopoulos<sup>1</sup> · Bernhard Weigand<sup>1</sup>

Received: 6 October 2021 / Accepted: 23 June 2022 / Published online: 5 August 2022  
© The Author(s) 2022

## Abstract

This paper reports on particle image velocimetry (PIV) measurements in compressible accelerated wake flows generated by two different central injector types, which are mounted in a convergent-divergent nozzle. The injectors differ by the extent of their trailing edge located either in the subsonic (injector A) or supersonic flow region (injector B). In addition, the undisturbed nozzle flow without injector is studied as a reference case. The PIV results reveal typical wake flow structures expected in subsonic (injector A) and supersonic (injector B) wake flows. They further show that the Reynolds stresses  $Re_{xx}$  and  $Re_{yy}$  significantly decay in all three cases due to the strong acceleration throughout the nozzle. Interestingly, in the case of injector A, the flow stays non-isotropic with  $Re_{yy} > Re_{xx}$  also far downstream in the supersonic flow region. These measurements were motivated by the lack of velocity data needed to validate numerical simulations. That is why this paper additionally contains results from (unsteady) Reynolds-averaged Navier-Stokes ((U)RANS) simulations of the two wake flows investigated experimentally. The URANS simulation of the injector A case is able to accurately predict the entire flow field and periodic fluctuations at the wake centerline. However, in the case of injector B, the RANS simulation underestimates the far wake centerline velocity by about 4%.

## 1 Introduction

Efficient and rapid mixing of two or multiple substances has been of scientific interest throughout the last decades motivated by various industrial applications, such as premixing the inflow for e.g. annular combustion chambers, (sc)ramjets, and chemical reactors. In many of these applications, continuous parallel mixing of fast flowing gases is implemented by utilizing a central injector. This involves a wake flow downstream of the injector's trailing edge, whose flow structures decisively determine the time and quality of mixing. That is why many researchers have studied such wake flows for many years. However, investigations have been conducted mostly for purely sub- or supersonic wake flows. In the case of subsonic flow, the wake that develops downstream of the central injector is

---

✉ Judith Richter  
judith.richter@itlr.uni-stuttgart.de

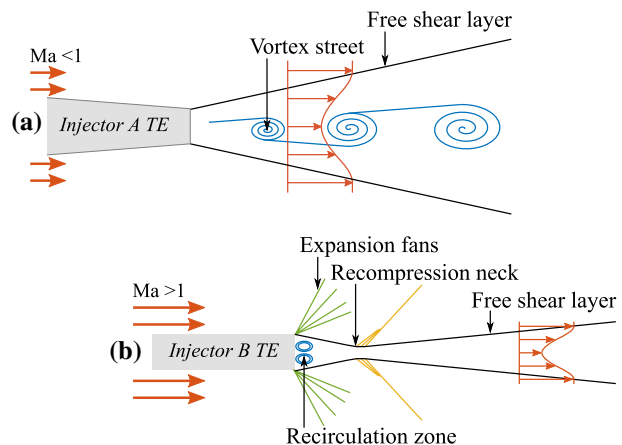
<sup>1</sup> Institute of Aerospace Thermodynamics, University of Stuttgart, Pfaffenwaldring 31, 70569 Stuttgart, Germany

dominated by large-scale alternating vortices (see Fig. 1a) known as the von Kàrmàn vortex street (Roshko 1953; Gerrard 1966). In particular, while the shear layer rolls up at one side, the shear layer from the other side is drawn across the wake centerline, thus, forming a subsequent vortex. As a consequence, the supply of vorticity to the growing vortex is reduced (Gerrard 1966). Various studies have shown that the vortex shedding frequency scales with the main flow velocity over a wide Reynolds number range (Roshko 1954; Goldstein 1950). Furthermore, normalized velocity profiles were shown to attain self-similarity in the far wake regardless of the geometry of the wake generator (Wynanski et al. 1986; Wohler et al. 2014; Richter et al. 2019). This also holds under varying pressure gradients (Liu et al. 2002; Beuting et al. 2018a).

In the case of supersonic wake flow, compressibility stabilizes turbulent diffusion and, thus, restrains the wake growth rate (Papamoschou and Roshko 1988; Barre et al. 1994; Smits and Dussauge 2006). It has been experimentally demonstrated that compressibility effects have an attenuating impact on the growth rate of the shear layers and the turbulent structures (Papamoschou and Roshko 1988; Barre et al. 1994). In addition, the characteristics of supersonic flow are fundamentally different from those of subsonic flow regarding the direction of the information flows and the reaction to changes in pressure as sketched in Fig. 1b. In particular, expansion fans are formed at the injector's trailing edge followed by an expansion and recompression zone, from which two oblique shock waves leave (Nakagawa and Dahm 2005; Amatucci et al. 1992). Despite these huge physical differences both, subsonic and supersonic wake flows, have in common that the flow profiles attain a self-similar state at a sufficient distance downstream from the wake generator (Nakagawa and Dahm 2006).

Whereas many wake flow investigations have been conducted in either subsonic or supersonic co-flows, wake flows in transonic co-flows, that pass through the transonic flow regime, are still largely unexplored. Few studies have been conducted focusing on the transonic flow around turbine blades. These studies, though, have investigated the influence of the vortex shedding frequency on redistribution of pressure and temperature within the wake near field (Carscallen et al. 2009, 1996). Results have shown that the strength and the point of vortex shedding depend on the injection quantity and that vortex shedding can be even completely suppressed by sufficient injection (Motallebi and Norbury 1981). More recent,

**Fig. 1** Typical flow structures of **a** subsonic wakes (*Injector A*) and **b** supersonic wakes (*Injector B*)



investigations on transonic wakes have been performed in order to develop a shock-wave flow reactor to synthesize nanoparticles (Wohler et al. 2014; Grzona et al. 2009; Chun 2009; Winnemöller et al. 2010, 2015). In such reactors, the precursor gas is injected in the subsonic region of a Laval nozzle. The cold mixing of the precursor with the gas-dynamically cooled co-flow avoids uncontrolled nanoparticle growth. The decomposition of the precursor is then activated globally by a shock wave and the associated jump in temperature. Previous laser-induced fluorescence (LIF) studies in our lab have demonstrated that, despite the extreme conditions within a strongly accelerated transonic nozzle flow, the self-similarity of the injectant concentration is preserved regardless of the injection angle, the shape of the central injector (with/without ramps), the flow Reynolds number as well as the imposed pressure gradient (Wohler et al. 2014; Beuting et al. 2018a; Chun 2009). Furthermore, different measurement techniques have been applied in order to provide an experimental data set that can be used for the validation of numerical simulations (Richter et al. 2019; Beuting et al. 2018b; Richter et al. 2018). This includes measurements of wake growth rates, concentration profiles, shedding frequency, Mach number, temperature and the identification of zones of micro/macro mixing. Recent numerical studies showed that unsteady Reynolds-averaged Navier-Stokes (URANS) simulations, incorporating the shear stress transport model by Menter (1994), can be used to predict such wake flows. In particular, numerical results obtained with URANS showed good agreement with laser-induced thermal acoustic (LITA) measurements of the temperature and Mach number distribution of an initially subsonic wake, which undergoes strong acceleration through a convergent-divergent nozzle (Richter et al. 2018). However, the same investigation revealed that the predicted velocity defect in the near field was about 17% smaller compared to LITA. This points to the complexity of the vortex formation mechanism and the associated lack of URANS to correctly predict the base pressure. This assumption was underpinned by an underestimation of the shedding frequency by 15%. In addition, numerical investigations have shown that the vortex formation mechanism strongly depends on the free-stream Reynolds number as well as the amount of injectant added to the wake (Richter et al. 2018). Thus, the accuracy of the experimental results used as validation data in numerical investigations is of central importance.

This paper aims to complement the existing data of transonic wake flows by performing 2D particle image velocimetry (PIV) experiments in the center-plane of two different transonic wakes that undergo strong acceleration in a convergent-divergent nozzle. The measured velocity field and turbulence statistics contribute to better understand such wake flows. Further, the complete data set (including the results of the present PIV experiments together with former LIF and LITA measurements) is valuable for the detailed validation of numerical simulations of future studies. In the present study, PIV experiments were carried out at the University of Stuttgart in a flow channel involving a convergent-divergent nozzle and optical access throughout the whole flow regime (subsonic–transonic–supersonic). Two different central injectors were utilized as wake generators to cover both cases sketched in Fig. 1: (initially) sub- and purely supersonic wake flow. In addition, an experiment was also carried out without an injector in order to accurately investigate the undisturbed nozzle flow as a reference case. Further, numerical results of (U)RANS simulations using the  $k$ - $\omega$ -SST turbulence model are provided as an example on how the obtained data may be used for validation. Thus, the focus of the present paper remains on the experimental findings because a detailed numerical study would be a topic for itself.

**Fig. 2** ITLR supersonic test facility

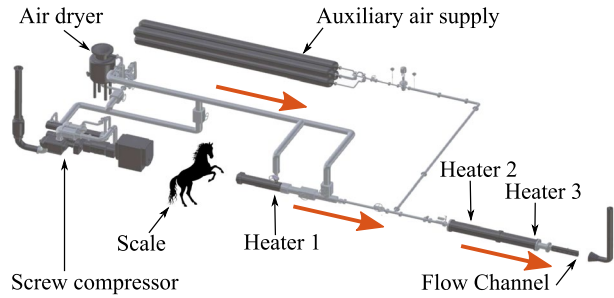
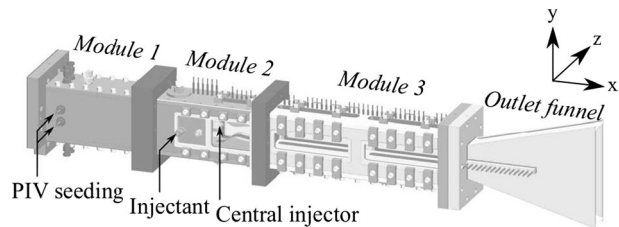


**Fig. 3** Modular, rectangular flow channel with a convergent-divergent nozzle designed for transonic mixing investigations



## 2 Experimental Methods

### 2.1 Experimental Setup

#### 2.1.1 Test Facility

Experiments were carried out at the supersonic test facility of the Institute of Aerospace Thermodynamics (ITLR) at the University of Stuttgart. The experimental test facility is depicted in Fig. 2. It consists of a screw compressor, which supplies air into a channel passing first an air dryer and three electrical heaters. Downstream of the flow channel, the exhaust air is discharged into the environment through a large chimney. Four compressed air tanks with a total capacity of 8 m<sup>3</sup> at 100 bar serve as an emergency air supply so that the heaters can be shut down in a controlled manner if the screw compressor fails. The system can compress ambient air up to 10 bar with a maximum flow rate of 1.45 kg s<sup>-1</sup> while the air can be heated up to 1500 K. A vortex mass flow meter (Endress + Hauser, Proirl 77H DN 100, accuracy < 1% of the measured value) and a pressure sensor (Omega, PAA21-C-10, accuracy < 0.5% of full scale), which measure the air mass flow rate and the total pressure at the inlet of the test section, are also installed.

#### 2.1.2 Flow Channel

The very same flow channel that was used for the present PIV investigations has already been used in previous studies (Richter et al. 2019; Beuting et al. 2018a, b; Richter et al. 2018). The modular flow channel is depicted in Fig. 3, for further details see (Richter et al. (2019)). It consists of three modules of rectangular cross-section with a constant width of 40 mm and a total length of 665 mm. The first module connects the heater with the optically accessible test section (modules 2 and 3). It is equipped with a seeding port that was utilized to add the particles required for the PIV measurements to the main flow (details see Sect. 2.3). A calibrated thermocouple (Type-K, accuracy  $\pm 1.5$ K), which is positioned

at the flow channel centerline, was used to measure the total temperature of the main flow. A wire mesh is located between module 1 and module 2 to dissolve large-scale turbulent structures evolving upstream from the heater or the injection device. For this purpose, a grid with 0.75 mm wire diameter and 2.0 mm mesh size is utilized. The second module comprises (optionally) a central injector and the convergent-divergent nozzle with a nozzle throat height of 26.3 mm. The nozzle is designed to accelerate air to a Mach number (definition see Eq. 6) of  $M = 1.7$ , for details on the nozzle geometry see Richter et al. (2018). Module 2 further provides an additional access port, which was not used for the present experiments. The third module has a constant height of 35.4 mm and is a planar extension of the second module that allows for the observation of the mixing layer development. Both, modules 2 and 3, provide optical access through quartz glass windows from all four sides. Furthermore, static pressure taps (Scanivalve, DSA 3016, accuracy  $< 0.05\%$  of full scale), are installed at the top wall to measure the wall pressure distributions in flow direction throughout the three modules.

Subject of the present investigation are transonic wakes generated by the central injector. Two different geometries of such are considered in this study. Both central injectors are drop-shaped and extend over the entire width of the channel. They vary only in the extension of their trailing edges as sketched in Fig. 4: Injector A extends to the nozzle entry, 42 mm upstream of its throat, whereas injector B reaches down into the supersonic flow region, 10 mm downstream of the nozzle's critical cross-section. Both trailing edges measure  $h_{ITE} = 5\text{ mm}$  in height and contain four exit holes of 2.5 mm in diameter with 4.8 mm distance from center to center. The injectant is fed laterally through the injector holding plates.

### 2.1.3 Flow Conditions

In all three cases, oil particles were added to the main flow through the seeding port located in the first module. The total temperature of the main flow was set to  $T_{0,\text{main}} = 380\text{ K}$  at the outlet of heater 3 (see Fig. 2). The total pressure was  $p_{0,\text{main}} = 2.5\text{ bar}$  for the cases of

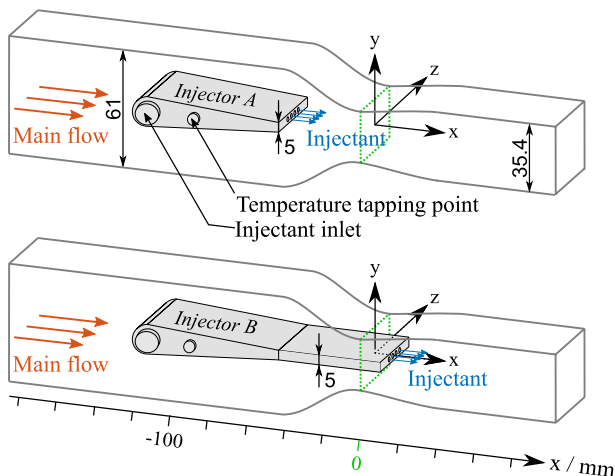
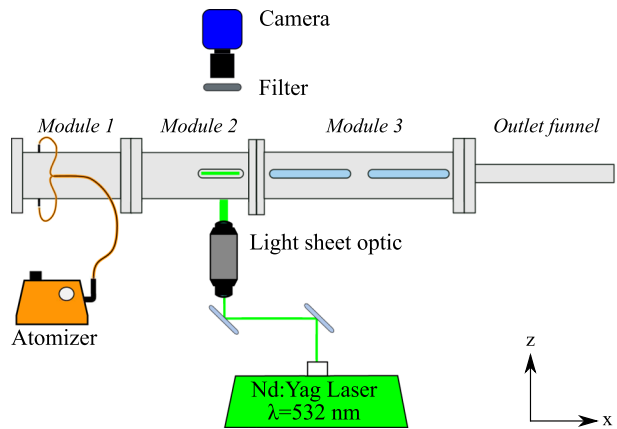


**Fig. 4** Geometry and position of the investigated wake generators/central injectors, as well as the location of the coordinate system in the center of the nozzle throat plane. All dimensions in mm

**Table 1** Flow conditions of the three cases investigated: undisturbed nozzle flow (nozzle), *Injector A* wake flow (InjA), and *Injector B* wake flow (InjB)

	$T_{0,\text{main}}$ (K)	$p_{0,\text{main}}$ (bar)	$\dot{m}_{\text{main}}$ ( $\text{gs}^{-1}$ )	$\dot{m}_{\text{inj}}$ ( $\text{gs}^{-1}$ )	$T_{0,\text{inj}}$ (K)
Nozzle	380	2.5	515	–	380
InjA	380	2.5	515	0.5	380
InjB	380	3.0	515	0.5	380

**Fig. 5** Schematic (top view) of the PIV setup



undisturbed nozzle flow and with injector A, whereas for the case of injector B was set to  $p_{0,\text{main}} = 3\text{bar}$  so that the main mass flow rate  $\dot{m}_{\text{main}}$  was maintained constant to compensate for the narrowed nozzle throat due to the extended trailing edge. The total temperature of the injectant  $T_{0,\text{inj}}$  was equal to  $T_{0,\text{main}}$ . In addition, the injectant mass flow rate  $\dot{m}_{\text{inj}}$  was adopted from LIF measurements (see Beuting et al. (2018b)). All flow conditions of the three cases investigated are summarized in Table 1.

## 2.2 Schlieren Imaging

In order to visualize the dominant wake flow structures, Schlieren imaging, which has been widely used to resolve such phenomena, was applied for the cases of injector A and B. The Schlieren experimental set up was identical to the one used in previous experiments (Richter et al. 2017) consisting of a point light source (green LED) triggered by a driver circuit (Menser et al. 2015), two achromatic lenses (focal length  $f = 1000\text{mm}$ ), an adjustable aperture, and an off-the-shelf single-lens reflex camera. The driver enabled an emission of a high-power short-time light pulse, where a light pulse of  $\Delta t = 5\mu\text{s}$  showed best results in terms of light output as well as blurring.

## 2.3 Particle Image Velocimetry (PIV)

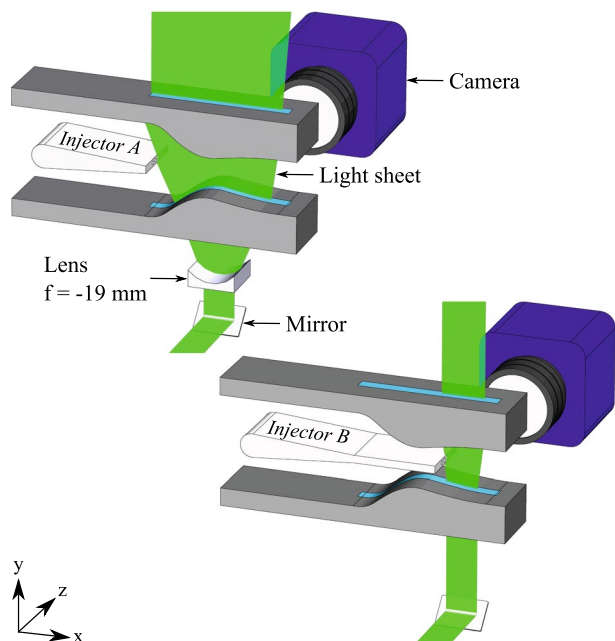
PIV was used to determine the velocity fields of all three cases (without and with injector A/B) in the mid- $x$ - $y$  plane of the flow channel, between the second and third injector bore, at  $z = 0\text{mm}$ . The experimental setup is shown in Fig. 5: The beam of a pulsed Nd:YAG laser (New Wave Research, Gemini PIV 200-15, wavelength  $\lambda = 532\text{ nm}$ ) was

formed into a laser light sheet that measured  $\Delta x \approx 70$  mm in width and  $\Delta z < 0.5$  mm in thickness. This light sheet was aligned along the mid- $x$ - $y$  plane as sketched in Fig. 6. Since the light sheet is deflected by the strong curvature of the nozzle, a correction lens was used to expose the subsonic flow region sufficiently.

The camera used was a 16-bit imager sCMOS from LaVision with a  $2560 \times 2160$  pixel image resolution and a maximum capture rate of 50 Hz whereas, the particles were produced of Di-Ethyl-Hexyl-Sebacat (DEHS) using an aerosol generator (Topas ATM 210). According to the manufacturer, the particle diameter is  $d_p < 1 \mu\text{m}$ . To distribute the particles evenly over the entire channel height, two circular injection pipes were used as sketched in Fig. 7 that inject the aerosol in the mid- $x$ - $y$  plane of module 1 through seven small slits each. The vortex shedding at the tubes causes very good mixing of the aerosol with the main flow.

All PIV measurements and evaluations were performed with the commercial software DaVis 8 from LaVision (LaVision 2011). The time difference between the two light pulses was chosen between  $\Delta t = 1 \dots 3 \mu\text{s}$  depending on the expected flow velocity, which corresponds to a mean particle shift of 3 to 10 pixel. At each measurement position, 1000 individual measurements were taken at 2 Hz. The vector calculation was done by cross-correlation functions with iterative reduction of the interrogation windows from  $64 \times 64$  pixel to  $32 \times 32$  pixel with two iterations, 90% overlap, and automatic weighting. In channel coordinates, the final interrogation window measures  $1.86 \times 1.86 \text{ mm}^2$  and the resolution of the data points is 0.19 mm. For further post-processing, only measuring points with a cross-correlation peak ratio of  $\text{CPR} \geq 100$  were considered and outliers were automatically eliminated by  $|\varphi - \bar{\varphi}| < 2\sigma_{\varphi}$ , where  $\varphi$  is either  $u$  or  $v$ , “ $\bar{\varphi}$ ” denotes a time-averaged quantity, and  $\sigma$  is the standard deviation. The resulting velocities were averaged over 250 individual measurements at each measurement point. Surplus measurement points were neglected to

**Fig. 6** 3D view of the light sheet illuminating the wake flow



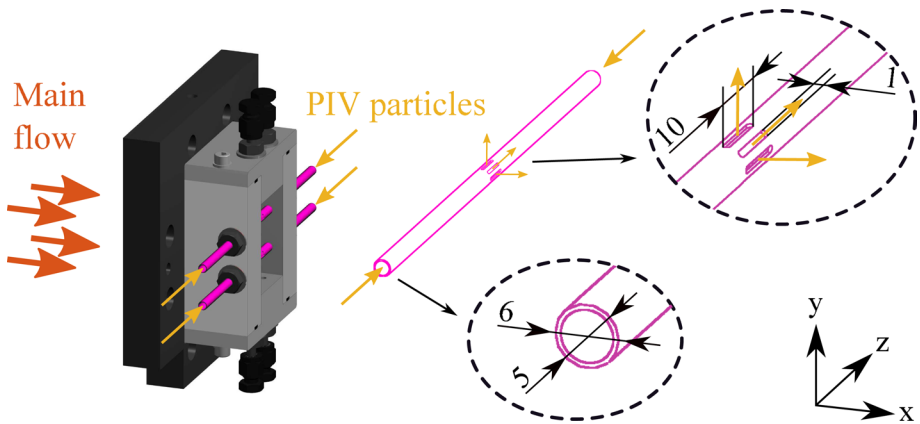


**Fig. 7** Injection pipes used for PIV seeding. All dimensions in mm

provide the same sample size everywhere because a varying sample size makes the interpretation of the statistical error difficult.

### 2.3.1 PIV Particle Response Time

How well the PIV particles follow the investigated flow is commonly evaluated by the Stokes number

$$St = \frac{\tau_p}{\tau_{\text{main}}}, \quad (1)$$

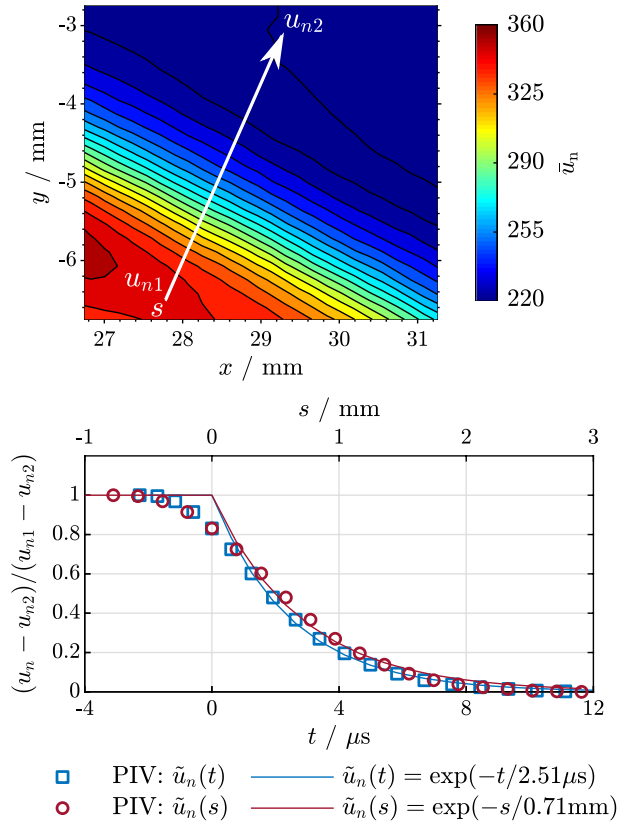
which is a dimensionless measure defined as the ratio of the relaxation time of a particle  $\tau_p$  and the characteristic time scale of the main flow  $\tau_{\text{main}}$ . Particle motion studies in turbulent compressible shear layers have shown that if  $St < 0.1$  the particles follow all small-scale movements (Krstić 2006; Samimy and Lele 1991).

In supersonic flows, the discontinuity of the flow velocity across an oblique shock wave (OSW) can be utilized to accurately determine  $\tau_p$  (Raffel et al. 2018; Scarano and Oudheusden 2003; Menter 1997; Ragni et al. 2011). As is common knowledge, the velocity decelerates abruptly across an OSW. Due to their inertia, the particles cannot depict this discontinuity of the flow velocity and, thus, react position- and time-delayed. In order to evaluate these delays, the distribution of shock-normal velocity  $u_n$  perpendicular to the shock wave, along the direction  $s$ , is required. This is illustrated in Fig. 8 by means of an OSW that is located downstream of injector B. Figure 8 also includes the corresponding normalized velocity  $\tilde{u}_n$  along the curve  $s$  as well as over the elapsed time  $t$ . An exponential curve fit (solid lines) yields a particle relaxation length  $\xi_p = 0.71$  mm and time  $\tau_p = 2.51 \mu\text{s}$ , which is similar to literature data (Scarano and Oudheusden 2003; Ragni et al. 2011) of similar cases.

The flow time scale  $\tau_{\text{main}}$  must be considered separately for injector A/B. In the case of injector A, the vortex shedding frequency, which measures 7.3 kHz (Richter et al. 2019), defines  $\tau_{\text{main,A}} = 137 \mu\text{s}$ . In the case of injector B, the time scale of a free shear layer  $\tau = 10\delta/\Delta u$  (Samimy and Lele 1991) can be utilized (Scarano and Oudheusden 2003), where a worst case scenario is chosen with  $\delta = 0.73$  mm being half the shear layer thickness



**Fig. 8** Particle response across a planar oblique shock wave (OSW): Velocity field of the shock-normal velocity component  $u_n$  (top) and corresponding normalized velocity  $\tilde{u}_n$  over the shock-normal abscissa  $s$  as well as elapsed time  $t = s/u_n$  and their exponential curve fits (bottom)



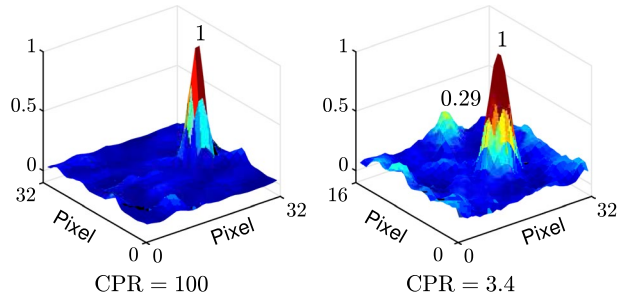
at the recompression neck and  $\Delta u = (459 - 70)\text{ms}^{-1}$  being the velocity difference at the point of injection. Accordingly,  $\tau_{\text{main,B}} < 18.8\mu\text{s}$ . Adopting this assessment,  $\text{St}_A = 0.02$  and  $\text{St}_B < 0.13$  and, thus, all flow structures of the present PIV measurements can be resolved.

### 2.3.2 PIV Measurement Uncertainty Estimation

In order to evaluate the measurement uncertainty both, the *systematic and statistical error*, have to be addressed. For the current case, the systematic error is mainly affected by common parameters of the PIV setup such as seeding density, out of plane motion, sound to noise ratio and correlation window size. According to Raffel et al. (2018) two methods to quantify the systematic error have become established in literature: The first one requires knowledge of the effect of all individual parameters on the overall uncertainty. The second one considers the correlation functions only, which are a result of all parameters and their contribution to the uncertainty.

The latter is based on the cross-correlation peak ratio CPR that is the ratio of the height of the largest to the second largest correlation peak. Figure 9 shows the results of two example correlation functions of two image pairs each (interrogation window  $32 \times 32$  pixel) with different CPR. Charonko and Vlachos (2013) showed that for  $\text{CPR} \geq 2$  the root mean square displacement error already drops significantly. They studied the relation between CPR and the displacement error  $u_{\vec{d}}$  by means of three artificial PIV signals

**Fig. 9** Typical cross-correlation functions with a unique solution (left) and increased signal-to-noise with still strong correlation (right), evaluated by means of the cross-correlation peak ratio CPR



representing different flow phenomena and deduced a relation  $u_d(CPR)$ . For the present investigations, only results with  $CPR \geq 100$  were considered for post-processing. This strict criterion could be applied with about 50% scrap and was chosen to guarantee the best possible measurement accuracy. For the current case, the formulation by Charonko and Vlachos yields an *systematic error* of  $< 0.5\%$  (a minimum total shift of 3 pixels as a basis).

The number of individual measurements considered for averaging has a significant influence on the accuracy of the time-average, i.e. the statistical error. How large the sample size  $N_{SP}$  has to be chosen in order to achieve the desired accuracy depends on the temporal fluctuations of the measured flow quantities and therefore depends on the flow phenomenon under investigation. In order to estimate the  $N_{SP}$  required in each case, Uzol and Camci (2001) proposed the following method: From the total individual measurements  $N_{SP,max}$  of a flow quantity  $\varphi$ , 100 randomly selected, statistically independent average values from  $N_{SP} \leq N_{SP,max}/2$  samples are taken to calculate a time-average  $\bar{\varphi}$ :

$$\bar{\varphi}_{N_{SP}} = \frac{1}{N_{SP}} \sum_{i=1}^{N_{SP}} \varphi_i \tag{2}$$

Then the dispersion of the calculated mean values

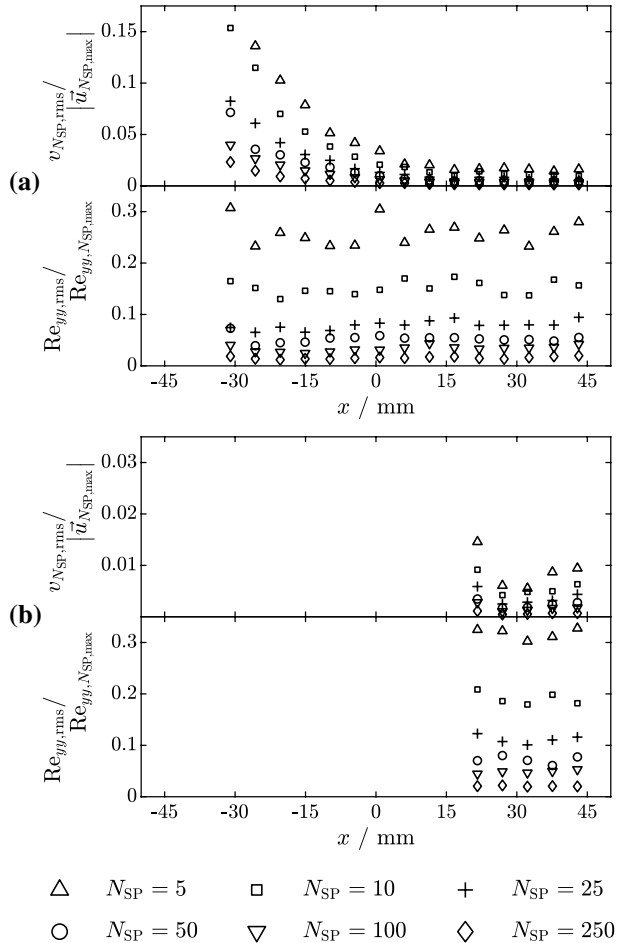
$$\bar{\varphi}_{N_{SP},rms} = \sqrt{\frac{1}{100} \left( \sum_{j=1}^{100} \bar{\varphi}_{N_{SP},j} - \bar{\varphi}_{N_{SP,max}} \right)^2} \tag{3}$$

is a measure of the accuracy of the time-average due to the selected  $N_{SP}$ . This procedure is repeated for a number of chosen  $N_{SP}$ .

In order to investigate how  $N_{SP}$  affects the time-averaging of the present PIV measurements, Eq. (3) was evaluated by means of the velocity components  $u$  and  $v$  as well as the Reynolds stresses (Eq. 8)  $Re_{xx}$  and  $Re_{yy}$  with  $N_{SP,max} = 500$  and  $N_{SP} = 10, 25, 50, 100, 250$ . Three different horizontal lines ( $y = 0, 2.5, 5\text{mm}$ ) within the nozzle ( $-45\text{mm} < x < 45\text{mm}$ ) were considered in order to identify the worst case scenario, which was located at the centerline ( $y = 0\text{mm}$ ). The normalized results are shown in Fig. 10, where only the dispersions of  $\bar{v}$  and  $Re_{yy}$  are plotted because the fluctuations in  $y$ -direction were dominant (cf. Fig. 17) and, thus, dictate the required sample size.

As expected, the dispersions of  $\bar{v}$  and  $Re_{yy}$  decrease with increasing  $N_{SP}$ . This means that the statistical error of the present PIV measurements can be reduced by choosing an appropriate large  $N_{SP}$ . In the case of injector A  $\bar{v}$  scatters strongly close to the trailing edge. This directly results from the periodic character of the wake, which requires a larger  $N_{SP}$  to accurately predict the time-average of the measured velocities. As the flow accelerates throughout

**Fig. 10** Sample size validation based on the  $v$  velocity component and Reynolds stress  $Re_{yy}$  for **a** *Injector A* and **b** *Injector B*



the nozzle, the influence of  $N_{SP}$  quickly diminishes. Besides, the choice of  $N_{SP} = 250$  significantly reduces the statistical errors. On the contrary, the scattering of  $Re_{yy}$  is independent of the  $x$ -position. Nevertheless, the statistical error can be also reduced to a similar low level when considering 250 samples for time-averaging.

The main findings from the injector A wake flow also apply to the injector B wake flow. As a result, the choice of  $N_{SP} = 250$  yields very accurate time-averaged flow properties ( $\bar{u}$ ,  $\bar{v}$ ,  $Re_{xx}$  and  $Re_{yy}$ ) with statistical errors of < 2%. Thus, the total measurement accuracy (systematic and statistical error) of the present PIV measurements accounts to < 2, 5% everywhere for both, the flow velocities as well as the Reynolds stresses. This corresponds to a total measurement uncertainty of < 3, 5  $ms^{-1}$  for  $\bar{u}$  and  $\bar{v}$  composed of < 2.5  $ms^{-1}$  systematic and  $\approx 1 ms^{-1}$  statistical error. Please note that the measured standard deviations of the flow velocities not only originate from the statistical error, but also from turbulent and periodic oscillations of the wake flow, i.e.

$$\sigma_{\bar{\varphi}} = \sigma_{\bar{\varphi},\text{statistical}} + \sigma_{\bar{\varphi},\text{periodic}} + \sigma_{\bar{\varphi},\text{turbulent}} \tag{4}$$

Since  $\sigma_{\varphi}$  was at least one magnitude larger than  $\sigma_{\varphi,\text{statistical}}$  in all of our measurements,  $\sigma_{\varphi}$  is a sound measure of the turbulent and periodic flow oscillations in this case. That is why in the following figures, the plotted error bars represent these flow variations, while the measurement accuracy is not shown because it is comparatively low.

### 3 Numerical Methods

Numerical investigations were performed with ANSYS CFX 19.0 (ANSYS 2019) for all three cases by solving the (U)RANS equations using the  $k-\omega$ -SST turbulence model developed by Menter (1994). Unsteady simulations were only feasible for the case of injector A, because the flow structures in the supersonic wake of injector B feature significantly smaller time scales. Subsequently, with the computational resources available for the present study, no time-resolved simulation was possible for the injector B case.

Figure 11 illustrates the hybrid meshes enclosing injector A and B, respectively. The mesh of the undisturbed nozzle flow case is similar to the injector B case but without the grid refinement in the wake flow region. The numerical domain was limited ( $-180 \text{ mm} \leq x \leq 200 \text{ mm}$ ) in flow direction, which represents module 2 and approximately one third of module 3. In addition, in the timely-resolved configuration with injector A, only a single injection bore of the central injector is considered in  $z$ -direction ( $\Delta z = 4.8 \text{ mm}$ ) to reduce the computational cost (Richter et al. 2019). For the cases with

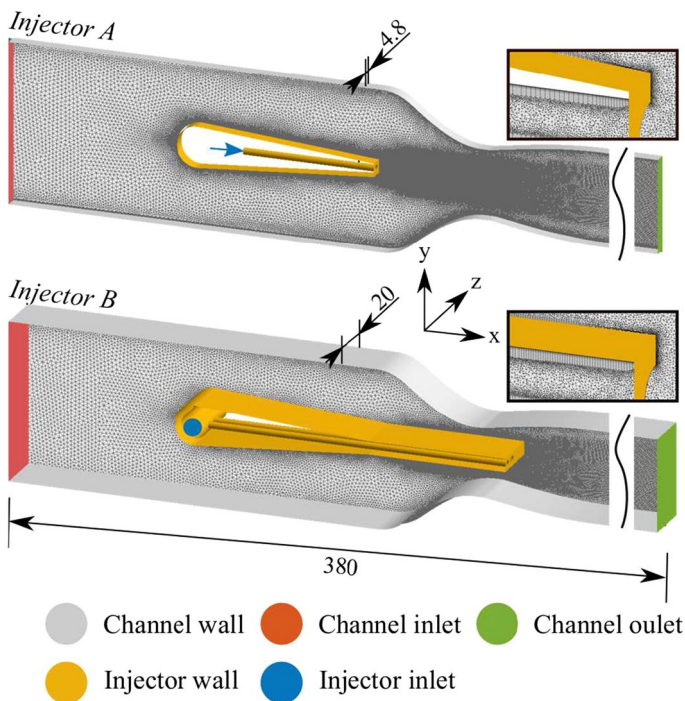


**Fig. 11** Sketch of the 3D numerical domain including the positions of applied boundary conditions and a section plane of the hybrid mesh of *Injector A* and *Injector B*. All dimensions in mm

injector B and without injector, the half channel ( $\Delta z = 20 \text{ mm}$ ) could be considered as the simulations were considered stationary. A grid sensitivity study was conducted to define an appropriate number of nodes  $N_{\text{nodes}}$  for each case that involved two steps: Firstly, the number of nodes clustered in the wake region was increased by factor 2 and 4. Secondly, the influence of the wall resolution at the central injector was studied in terms of the dimensionless wall distance  $y_{1,\text{inj}}^+ = u^* y_1 / \nu$ , where  $u^*$  is the friction velocity,  $\nu$  the kinematic viscosity and  $y_1$  the height of the first cell near the wall. In addition, the time step  $\tau_{\text{URANS}}$  was doubled to ensure an appropriate time resolution (applies only to the injector A setup). The resulting  $N_{\text{nodes}}$ ,  $y_{1,\text{inj}}^+$  and  $\tau_{\text{URANS}}$  of this assessment are summarized in Table 2. All of these yield an overall relative error  $< 1\%$  of the velocity field compared to the respective next closest setup. Wall functions were applied everywhere, where  $y_{1,\text{inj}}^+ > 30$ .

All flow channel and injector walls were treated as no-slip, smooth walls. Periodic boundary conditions were applied to the sidewalls of the injector A setup, and the center planes of both other setups were defined as symmetry planes. Profiles of total pressure, turbulence intensity, and eddy viscosity ratio were applied as channel inlet boundary conditions, together with an inlet (constant) total temperature. 3D RANS simulations that covered module 1 were performed to provide the required profile data (Richter et al. 2019). In this preliminary simulations, the boundary conditions of the experimental flow conditions ( $\dot{m}_{\text{main}}$ ,  $T_{0,\text{main}}$ ) and wall static pressure at the test section inlet ( $p_{\text{main}}$ ) were applied together with an inlet turbulence intensity  $Tu$  of 5% and an inlet eddy viscosity ratio  $\nu_t/\nu$  between the turbulent and molecular dynamic viscosity of 100 to determine the subsonic flow conditions at the channel inlet. At the channel outlet, the supersonic boundary condition of ANSYS CFX was applied, where all dependent variables are extrapolated from the flow conditions upstream (ANSYS 2019). At the injector inlet,  $\dot{m}_{\text{inj}}$  was set to 1/4 (injector A) or 1/2 (injector B) of the experimental condition (assuming even mass flow distribution over all four injector bores) and  $T_{0,\text{inj}} = 380\text{K}$ .

### 4 Results and Discussion

The following chapter is organized in four sections: First, the general flow features are presented in Sect. 4.1. This includes the characteristic flow properties, the characteristic flow structures and the wall static pressure distribution of all three cases. Sections 4.2, 4.3 and 4.4 comprise a detailed discussion of the PIV measurements, where a separate section is devoted to each of the topics of *undisturbed nozzle flow*, *injector A wake flow* and *injector B wake flow*.

**Table 2** Details of the numerical setups of the *undisturbed nozzle flow* (nozzle), *Injector A* (InjA), and *Injector B* (InjB)

	Method	$\Delta z$	$N_{\text{nodes}}$	$y_{1,\text{channel}}^+$	$y_{1,\text{inj}}^+$	$\tau_{\text{URANS}}$
	(–)	(mm)	( $\times 10^6$ )	(–)	(–)	( $\mu\text{s}$ )
Nozzle	RANS	20	11.37	$> 30$	–	–
InjA	URANS	4.8	5.35	$> 30$	$< 1$	0.5
InjB	RANS	20	34.39	$> 30$	$> 30$	–

## 4.1 General Flow Features

### 4.1.1 Flow Properties

The appropriate definition of characteristic dimensionless numbers such as Reynolds ( $Re$ ) and Mach number ( $M$ ) is essential because strong acceleration causes large gradients within the nozzle. In the present study,  $Re$  and  $M$  were obtained either at the boundary layer edge above the injector's trailing edge (index: ITE) or at the nozzle exit (index: NE).  $Re$  is calculated from Eq. (5), where  $\rho$ ,  $\bar{u}$  and  $\eta$  are the density, averaged velocity and dynamic viscosity, respectively.  $L$  refers to a characteristic length that is the height of the injector's trailing edge  $h_{ITE} = 5$  mm or the hydraulic diameter at the nozzle exit  $d_{h,NE} = 9.39$  mm. Equation (6) defines  $M$ , where  $\bar{u}$  and  $c$  are the averaged velocity and the speed of sound.

$$Re = \frac{\rho \bar{u} L}{\eta} \quad (5)$$

$$M = \frac{\bar{u}}{c} \quad (6)$$

Table 3 summarizes  $Re$  and  $M$  of all the three cases investigated obtained from results of the corresponding (U)RANS simulations. In the case of injector B, the height of the nozzle throat is decreased due to the extended trailing edge, and as a consequence,  $M_{NE}$  is increased.

### 4.1.2 Flow Visualization (Schlieren Imaging)

Short-time illuminated Schlieren imaging was performed in order to identify the wake flow structures, sketched in Fig. 1, for the cases of injector A/B. Even though the photographs reveal nothing unexpected, Fig. 12 is used to briefly discuss the physics of the wake flows as a basis of the following discussions:

The Schlieren image of the injector A wake flow nicely visualizes the vortices that shed from the trailing edge. These oscillate at a frequency of 7.3 kHz (Richter et al. 2017) and, thus, can only be resolved if the illumination time is sufficiently short. The vortices merge with the background within only few millimetres downstream of the injector trailing edge because the density fluctuations, which are visualized by the Schlieren technique, quickly dissolve as the wake develops. In addition, the Schlieren image of injector A nicely pictures some of the general nozzle features: starting at the nozzle throat, expansion fans evolve that should be ideally cancelled out by the nozzle contour when hitting the walls. However, a weak shock system downstream of the

**Table 3** Reynolds numbers ( $Re$ ) and Mach numbers ( $M$ ) at the injector's trailing edge position (index ITE) and at the nozzle exit (index NE) of the three cases investigated: *undisturbed nozzle flow* (nozzle), *Injector A* (InjA), and *Injector B* (InjB)

	$Re_{ITE} \times 10^5$	$M_{ITE}$	$Re_{NE} \times 10^5$	$M_{NE}$
Nozzle	–	–	2.17	1.70
InjA	0.63	0.35	2.17	1.70
InjB	1.70	1.43	2.25	1.95

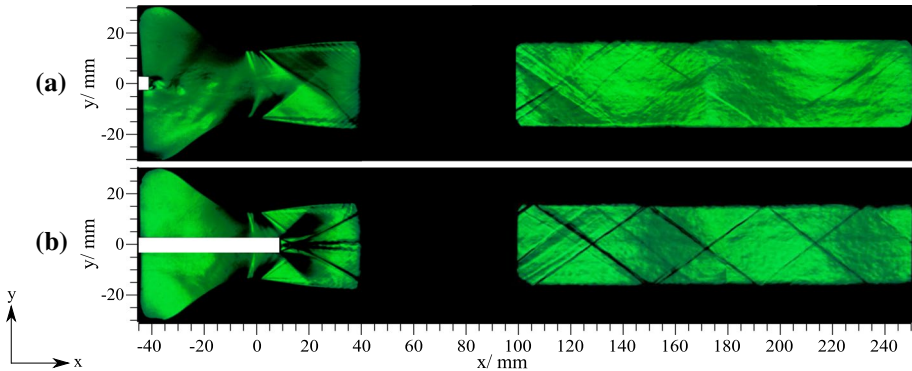


**Fig. 12** Short-time illuminated Schlieren images of both investigated injector configurations, **a** *Injector A* and **b** *Injector B*. Injector trailing edges are marked white at the very left edges. In the area  $40\text{ mm} \leq x \leq 100\text{ mm}$  no windows are present (see Fig. 3)

nozzle in the second viewing window ( $x > 100\text{ mm}$ ) proves that this is not the case. Nevertheless, the oblique shocks are weak and the nozzle is well designed.

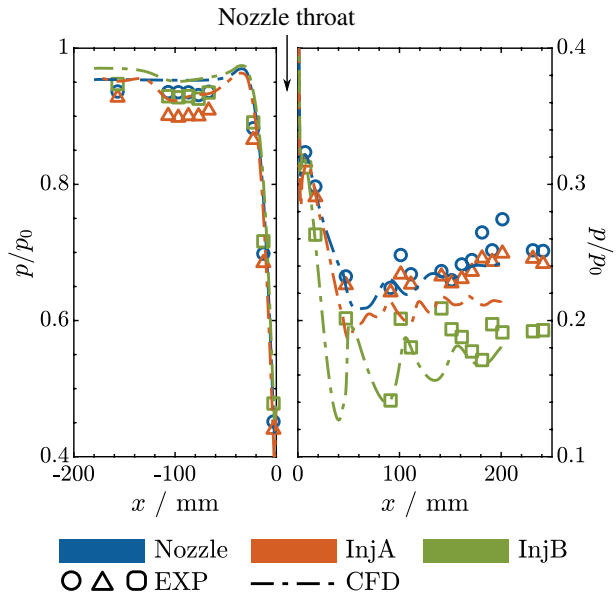
In the Schlieren image of injector B the flow characteristics of a supersonic wake flow, cf. Fig. 1b, are most dominant. The large dark colored areas at the upper/lower corners of the trailing edge nicely depict the expansion fans. The two visible lines, which start from the recompression neck at about  $x = 20\text{ mm}$ , hit the channel walls and continue within the second window ( $x > 100\text{ mm}$ ), display the two oblique shock waves and their reflections. The Schlieren image also clearly pictures the wavy structure of the highly turbulent shear layers in the first window ( $x > 20\text{ mm}$ ). However, in the second window these coherent structures have been dissolved. Apparently, these vortices decay into small-scale eddies at higher frequencies that the used Schlieren setup cannot capture.

#### 4.1.3 Wall Pressure Distribution

Figure 13 depicts the static wall-pressure distribution normalized by the inlet total pressure  $p_{0,\text{main}}$  (see table 1). The results nicely reveal the strong acceleration through the convergent-divergent nozzle for all three cases. In the case of injector B, the flow is comparatively further accelerated, due to the narrowing of the nozzle throat (see Table 3). Furthermore, the reflection of shock waves originating from the recompression neck at the channel walls (see Fig. 12) causes periodic pressure conditions, which are clearly observed in Fig. 13. The positions of the local maxima of static pressure coincide with the crossing points of the reflected shock waves at the center line (see Fig. 12b). At these crossing points, the flow is locally compressed, which explains the local increase in static pressure. Figure 13 also reveals that the simulations are able to predict the pressure conditions very well throughout the whole flow channel.

In addition, calculations assuming 1D, isentropic flow conditions (entropy  $S = \text{const.}$ ) identify  $M_{S=\text{const}}$  and  $u_{S=\text{const}}$  through the nozzle to provide expected conditions for a plausibility check and normalization of velocities:

**Fig. 13** Normalized wall static pressure distribution of the *undisturbed nozzle flow* (Nozzle), *Injector A* (InjA) and *Injector B* (InjB) from measurements (EXP) and numerical simulations (U RANS)



$$\left(\frac{p_0}{p}\right)_{S=const.}^{\frac{\gamma}{\gamma-1}} = \left(\frac{T_0}{T}\right)_{S=const.} = 1 + \frac{\gamma-1}{2} M_{S=const.}^2 \tag{7a}$$

$$u_{S=const.} = M_{S=const.} \sqrt{\gamma R T_{S=const.}} \tag{7b}$$

From this assessment, a nozzle exit Mach number of  $M_{NE} = 1.6$  is calculated, which is slightly lower than the nozzle designed Mach number of  $M_D = 1.7$ . However, previous LITA measurements (Richter et al. 2018) have proven that  $M_D$  is reached at the nozzle center line. This difference can be justified by losses in  $p_{0,main}$ , so that  $p/p_0$  is actually higher than assumed.

## 4.2 Undisturbed Nozzle Flow

### 4.2.1 Time-Averaged Centerline Velocity

PIV measurements were carried out in the undisturbed convergent-divergent nozzle flow to study the main flow conditions without injector and to provide reference data. Figure 14 shows the measured velocities  $\bar{u}_{CL}$  and  $\bar{v}_{CL}$  along the nozzle centerline (index: CL) from the current PIV experiments and RANS simulations together with previous findings from LITA measurements (Richter et al. 2018). Strong acceleration through the convergent-divergent nozzle flow can be clearly observed. The LITA results seem to be slightly shifted upstream, which might be due to difficulties in the alignment of the flow channel. Overall, excellent agreement between the two experimental methods (LITA, PIV) as well as the RANS simulations is seen. However, the streamwise velocity at the nozzle exit is about 10% higher than it was expected based on the 1D isentropic calculations. As mentioned before, this can be attributed to losses



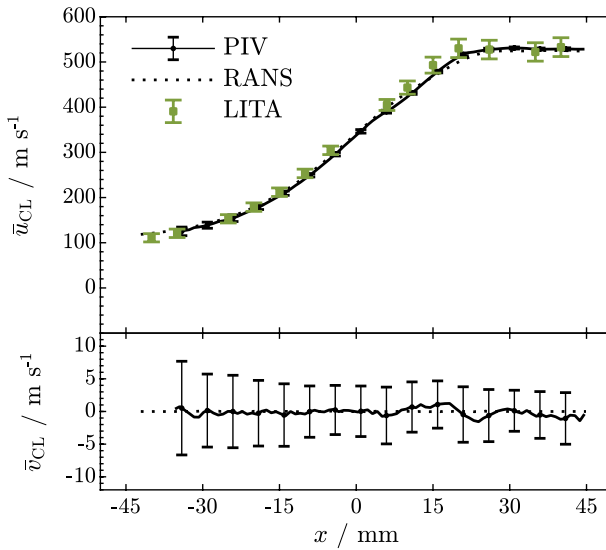


**Fig. 14** Measured (PIV, LITA) and predicted (RANS) velocity components  $\bar{u}_{CL}$  and  $\bar{v}_{CL}$  along the nozzle centerline ( $y = z = 0\text{mm}$ ) of the *undisturbed nozzle flow*. The bars denote velocity fluctuations due to turbulent oscillations. For details on the reference data from laser-induced thermo acoustic (LITA) measurements see (Richter et al. 2018)

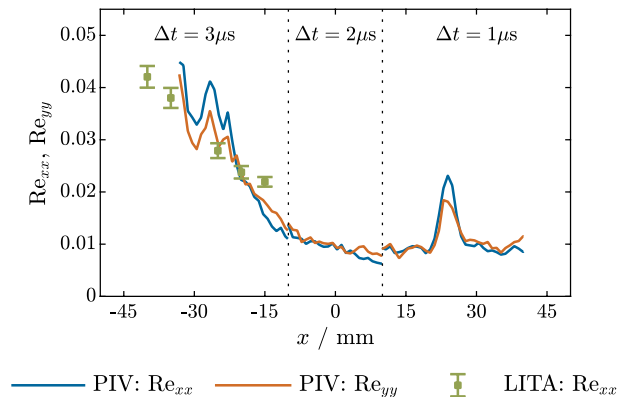
in total pressure, which falsify the assesment based on the isentropic flow assumption (as discussed above), and to boundary layer effects, which reduce the effective cross-section.

### 4.2.2 Turbulence Statistics

Figure 15 depicts the normalized Reynolds stresses

$$Re_{xx} = \frac{u'_{rms}}{u_{S=const}}, Re_{yy} = \frac{v'_{rms}}{u_{S=const}} \tag{8}$$

**Fig. 15** Measured, normalized specific Reynolds stresses  $Re_{xx}$  and  $Re_{yy}$  of the *undisturbed nozzle flow* along the channel center line ( $y = z = 0\text{mm}$ ). PIV data are recorded with optimized time differences between the light pulses  $\Delta t$  depending on the mean flow velocity. For details on the reference data from laser-induced thermoacoustic (LITA) measurements see Richter et al. (2018)



derived from PIV as well as LITA measurements (Richter et al. 2018), where  $u'_{\text{rms}}$  and  $v'_{\text{rms}}$  are the root mean square of the fluctuating (periodic and turbulent) part of the velocity with  $\varphi' = \varphi - \bar{\varphi}$ , and  $u_{S=\text{const}}$  is the local velocity from 1D isentropic calculations (Eq. 7). Since  $u_{S=\text{const}}$  ranges between 100 to 500  $\text{ms}^{-1}$  the optimum time difference between the two light pulses  $\Delta t_{\text{opt}}$  depends on the position within the nozzle. In particular,  $\Delta t_{\text{opt}} = 1 \mu\text{s}$  applies to the nozzle exit area, whereas for the nozzle entry  $\Delta t_{\text{opt}} = 3 \mu\text{s}$ . That is why Fig. 15 contains results from three different PIV measurements with the respective  $\Delta t_{\text{opt}}$ , which are separated by vertical lines.

Both Reynolds stresses  $\text{Re}_{xx}$  and  $\text{Re}_{yy}$  strongly decay due to acceleration. Only exception is a local increase at about 27 mm. The results from numerical simulation (not shown here) reveal that at this location the expansion fans, which originate at the nozzle throat, cross the center line. In addition, results from LITA measurements confirm the trend of decaying  $\text{Re}_{xx}$  but show lower fluctuations through the nozzle flow. The LITA technique is based on the transport of an induced density grating and, thus, it is very susceptible to turbulence fluctuations. For that reason, it is prone to underpredict a high turbulence level.

### 4.2.3 Velocity Profiles

Normalized velocity profiles are shown in Fig. 16 for six different streamwise positions, where  $x = 0$  indicates the nozzle throat position. The results nicely show that, due to the strong acceleration from sub- to supersonic speed, a velocity deficit develops at the nozzle centerline. This velocity deficit, originating from the acceleration, is much stronger than the expected wake deficit. Due to the superposition of both, the velocity deficit caused by flow acceleration and the wake deficit generated by the central injector, the assessment of the wake deficit based on the velocity field was not possible. To thoroughly investigate the evolution of the wake deficit and the wake growth rate, LIF measurements exploiting a fluorescent injectant were performed in the past. The interested reader may thus be referred to former publications (Richter et al. 2019) that address this topic in detail, whereas the present paper focuses on the wake velocity field only. Furthermore downstream, the flat profile at the nozzle exit ( $x = 40 \text{ mm}$ ) indicates a well-designed nozzle. In addition, the predicted (RANS) velocity profiles agree very well with the measurements (PIV), meaning that all simulated values are within the range of turbulent fluctuations visualized as bars.

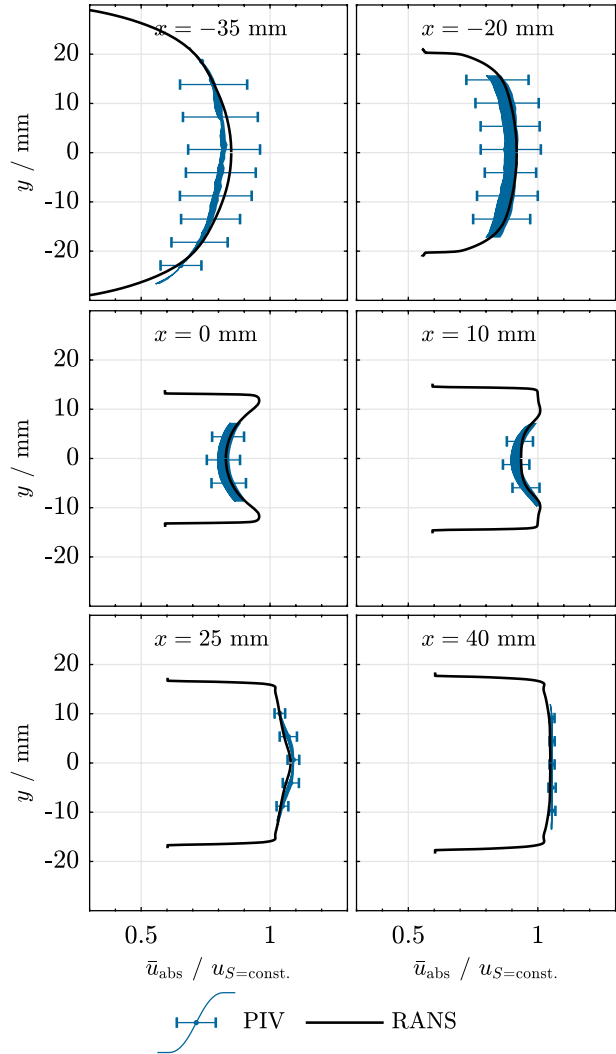
As discussed above, the plotted error bars are a measure of the periodic and turbulent flow oscillations  $u' = u'_{\text{periodic}} + u'_{\text{turbulent}}$  since they are at least one magnitude larger than the measurement uncertainty (cf. Eq. 4). Here, in the absence of vortex shedding, they represent  $u'_{\text{turbulent}}$  only. These turbulent fluctuations decrease significantly while the flow is accelerated to supersonic speed. This is in accordance with the drop of  $\text{Re}_{xx}$  and  $\text{Re}_{yy}$  (see Fig. 15).

## 4.3 Injector A Wake Flow

### 4.3.1 Time-Averaged Velocity

Figure 17 displays measured (PIV) and predicted (URANS) time-averaged velocities  $\bar{u}_{\text{CL}}$ ,  $\bar{v}_{\text{CL}}$  at the wake centerline of injector A within the nozzle and the first window of module 3. The steep increase of  $\bar{u}_{\text{CL}}$  clearly evidences the strong acceleration within the nozzle and how the wake deficit, caused by injector A, decays quickly within less than 22 mm. In particular,  $\bar{u}_{\text{CL}}$  is initially reduced by  $83.5 \text{ ms}^{-1}$  at the first measuring point ( $x = -36.5 \text{ mm}$ )

**Fig. 16** *Undisturbed nozzle flow*: Profiles of time-averaged absolute velocity  $\bar{u}_{\text{abs}}/u_{S=\text{const.}}$  normalized w.r.t. the isentropic flow velocity (Eq. 7) at different  $x$ -positions within the convergent-divergent nozzle. The bars denote velocity fluctuations due to periodic and turbulent oscillations



compared to the case of the undisturbed nozzle flow (plotted in grey) but catches up at  $x = -20$  mm, from where the two courses with/without injector match.

Downstream of the nozzle, within module 3 ( $x > 75$  mm),  $\bar{u}_{\text{CL}}$  slightly decays by about  $25 \text{ ms}^{-1}$  ( $-2.5\%$ ) within 150 mm. This deceleration can be accounted to a boundary layer thickening causing an adverse pressure gradient in combination with the constant cross-section of module 3 and to the weak shock system present throughout the entire flow channel in module 3 (see Fig. 12a). The former accounts for less than half of the deceleration, as indicated by the displacement thickness  $\delta^*$  of the numerical simulation, where  $\delta^*$  increases from 0.28 mm at the nozzle exit ( $x = 45$  mm) to 0.49 mm at the end of the numerical domain ( $x = 200$  mm). The latter also provides the explanation for the observed local oscillations of  $\bar{u}_{\text{CL}}$ .

Since the used PIV setup could not capture the second viewing window at once, different colors used in Fig. 17 refer to different colors used in Fig. 17 refer to different measurement positions, which nicely

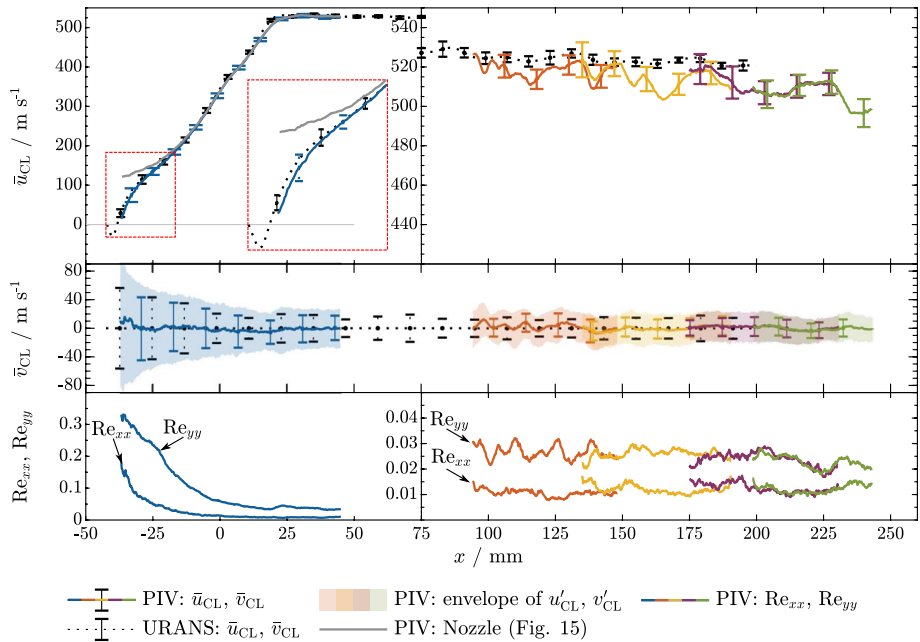


**Fig. 17** *Injector A wake flow*: Measured (PIV) and predicted (URANS) time-averaged velocity components  $\bar{u}_{CL}$ ,  $\bar{v}_{CL}$  and Reynolds stresses  $Re_{xx}$ ,  $Re_{yy}$  along the channel centerline ( $y = z = 0$  mm). The bars refer to the standard deviations  $\sigma_u$ ,  $\sigma_v$  originating from turbulent and periodic oscillations of the wake flow. Different colors refer to different (overlapping) measurement positions

overlap with deviations < 1%. This proves that the flow is quasi stationary because the measurement positions were recorded at different times (separated by several minutes). For the same reason, it further shows that the PIV measurements were repeatable.

The URANS simulation were able to accurately predict  $\bar{u}_{CL}$  (error < 1%) within the nozzle for  $x > -20$  mm, where the wake deficit has already disappeared. However, upstream of this point, closer to the injector’s trailing edge, the URANS simulation underestimates the wake deficit (error < 10%, see zoom in Fig. 17). Unfortunately, PIV measurements were not able to capture the recirculation zone in the near field of the injector A with the current PIV setup. This is due to the following two limitations: First, since the particles are fed into the main and not into the injector flow, the unmixed region in the vicinity of the trailing edge is not seeded. The injector flow was deliberately not provided with particles because the particle mass flow could not be controlled and, thus, could affect the wake flow in an uncontrolled manner. Second, the injector is made of copper and causes tremendous refractions so that the trailing edge was heavily overexposed. Within module 3 ( $x > 75$  mm) the predicted  $\bar{u}_{CL}$  is slightly higher than the measured and does not exhibit any oscillations. The authors contribute this to the reduced numerical domain in z-direction omitting the side walls and manufacturing inaccuracies of the nozzle contour.

Predicted (URANS) and measured (PIV) vertical velocity fluctuations  $v'_{CL}$  are depicted as bars in the second plot of Fig. 17. They are initially large due to the vortex street that forms at the injector A trailing edge (see Figs. 1 and 12a) and thus induces considerable periodic velocity fluctuations in y-direction. These fluctuations

quickly decay while the initially large vortices decompose into smaller eddies and the flow accelerates to supersonic speed. URANS simulation is able to correctly predict the amplitude of  $v'_{CL}$ , whereas it slightly underestimates  $u'_{CL}$ . Note that in the case of URANS simulations  $u'_{CL}$  and  $v'_{CL}$  only depict periodic fluctuations. From the fact that, despite this limitation, the velocity fluctuations are well predicted, the authors conclude that the periodic fluctuations are dominant while the turbulent fluctuations are comparatively minor. This has been observed before, e.g. in the periodic wake of a square cylinder (Ke 2019). A quantitative analysis of the share of periodic and turbulent fluctuations, however, would require time-resolved experimental data (e.g. from high-speed PIV or hot wire anemometry) to apply a Fourier transformation.

Further, the contour plot of the entire velocity field (Fig. 18) shows that not only the centerline velocities, but also the entire flow field is very well predicted by the URANS simulation with an overall deviation of  $< 5\%$  (Fig. 18c). The only difference would be that the flow field of the URANS (Fig. 18b) is perfectly symmetric, whereas local fluctuations were present in the experiment (Fig. 18).

### 4.3.2 Turbulence Statistics

Normalized Reynolds stresses ( $Re_{xx}$ ,  $Re_{yy}$ ) also depict the impact of the strong acceleration on the flow:  $Re_{xx}$  and  $Re_{yy}$  are initially extremely high due to periodic velocity fluctuations induced by the von Kármán vortex street. Both rapidly decay by more than one order of magnitude while the flow is accelerated to supersonic speed. Such rapid decay in turbulence intensity may cause a laminarization process in the wake and inhibit

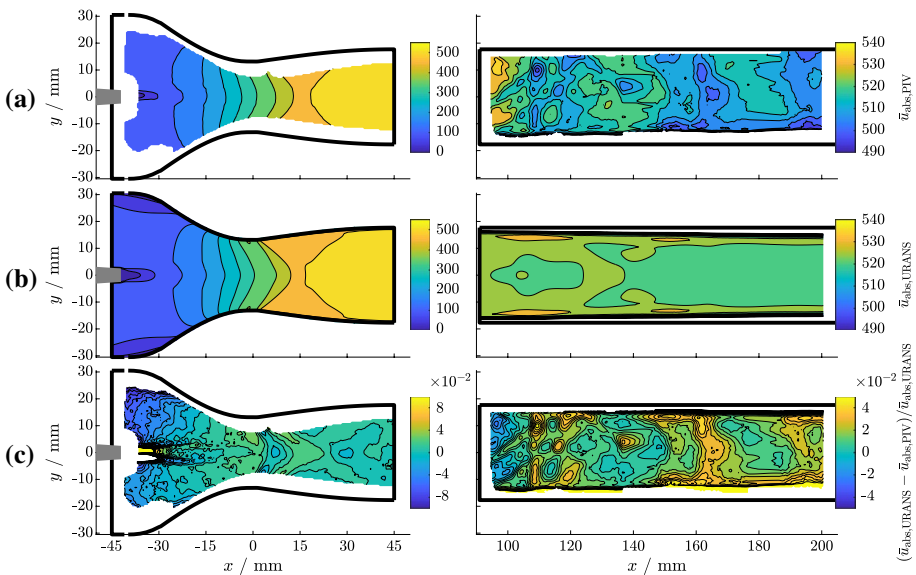


**Fig. 18** Injector A wake flow: Contour plots of time-averaged absolute velocity  $\bar{u}_{abs}$ ; **a** PIV measurements, **b** URANS simulation, and **c** relative deviation between PIV and URANS. The black frames outline the geometries of the two side windows; the injector trailing edge is sketched in gray

the mixing (Winnemöller et al. 2015). If laminarization occurs, this can be evaluated by means of the acceleration parameter

$$K = \frac{\eta}{\rho \bar{u}_{CL}^2} \frac{d\bar{u}_{CL}}{dx}. \quad (9)$$

Laminarisation becomes of significance if  $K > 2 \times 10^{-6}$ ; for  $K > 1 \times 10^{-5}$  the reversion to a laminar flow is considered to be complete (Yang and Tucker 2016). For the current cases,  $K_{\max} \approx 1.8 \times 10^{-6}$  within the convergent-divergent nozzle, thus, the flow stays turbulent. Nevertheless, this causes a strong decay in turbulence level.

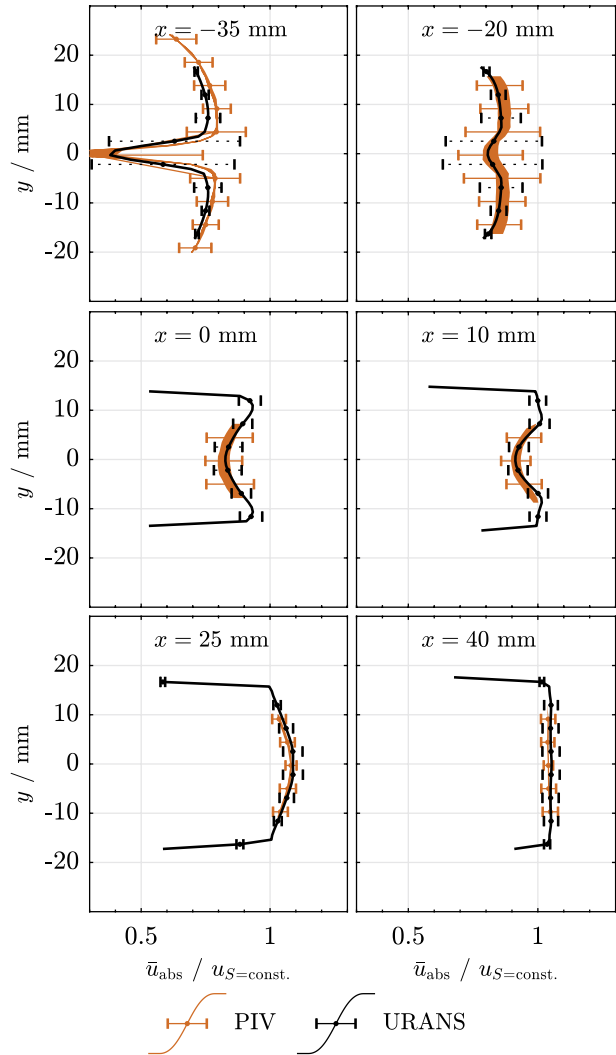
In the second viewing window, despite the strong acceleration,  $Re_{yy}$  remains about twice as high as  $Re_{xx}$ . This is remarkable because it seems that  $Re_{yy}$  withstands, meaning that the vortex shedding causes a non-isotropic flow field far downstream in the supersonic flow region. From this the authors conclude that the *streamwise acceleration* preliminary acts on the *streamwise normal stresses*, whereas the lateral normal stresses are less affected. This is in accordance with the rapid distortion theory (RDT) (Narasimha and Sreenivasan 1979), which applies to initially isotropic flows under a strong favorable pressure gradient. Here, turbulent eddies are “distorted”, resulting in a decrease of the normal stresses in the direction of the acceleration, while the lateral normal stresses may be further enhanced. However, in the current situation this effect is partly covered by the von Kármán vortex street entering the convergent divergent nozzle, which provides already dominant normal stresses at the inlet of the nozzle.

### 4.3.3 Velocity Profiles

Figure 19 depicts predicted (URANS) and measured (PIV) velocity profiles at different streamwise positions. An overall very good agreement between URANS simulations and PIV results is seen, meaning that all simulated values are within the spatial uncertainty of the PIV setup (marked by the line thickness). The only exception is the measurement position closest to the injector trailing edge, at  $x = -35$  mm, where the predicted deficit velocity deviates about 10%. This underpins our previous conclusions from LITA measurements (Richter et al. 2019). More specifically, LITA results showed that the centreline Mach number deficit was underestimated by the URANS simulation by about 17%. From this, one can conclude that the onset of vortex shedding is not entirely captured by our URANS. This shortcoming could neither be improved with a twofold finer grid resolution nor with halving the time step, both of which were investigated with a grid sensitivity study. Nevertheless, a much higher grid resolution and a much smaller time step combined with the appropriate computer resources maybe could improve the results.

A comparison with the velocity profiles of the undisturbed nozzle (see Fig. 16) shows that the wake deficit vanishes latest at the nozzle throat ( $x = 0$  mm). In addition, Fig. 19 nicely displays how the velocity profile flips due to the strong acceleration, indicating that the velocity deficit is much stronger than the wake deficit. Subsequently, an assessment of the wake deficit based on velocity profiles is highly difficult. That is why we assessed intensity profiles of LIF instead in our previous studies (Richter et al. 2019; Beuting et al. 2018a, b; Richter et al. 2016). From these we were able to prove the self-similarity of the wake flow.

**Fig. 19** *Injector A wake flow:* Profiles of time-averaged velocity  $\bar{u}_{\text{abs}}/u_{S=\text{const.}}$  normalized w.r.t. the isentropic flow velocity (Eq. 7) at different  $x$ -positions within the convergent-divergent nozzle. The bars denote velocity fluctuations due to periodic and turbulent oscillations



### 4.4 Injector B Wake Flow

#### 4.4.1 Time-Averaged Velocity

Figure 20 displays the measured (PIV) and predicted (RANS) velocities  $\bar{u}_{\text{CL}}$  and  $\bar{v}_{\text{CL}}$  in the wake of injector B. Unfortunately, no PIV results could be obtained upstream of  $x = 25$  mm for the same reasons discussed above for injector A (main flow seeding and light refraction), thus, missing the first 15 mm of the wake. That is why the recirculation zone, which typically forms in the very vicinity of a blunt body’s trailing edge in supersonic co-flow (see Fig. 1b), was not captured. In addition, the measured  $\bar{u}_{\text{CL}}$  at  $x > 25$  mm does not undergo further acceleration, meaning that the wake deficit has already caught up. This indicates that the recirculation zone must be short and, thus, sufficient mixing already took place until the first PIV measurement point only 15 mm

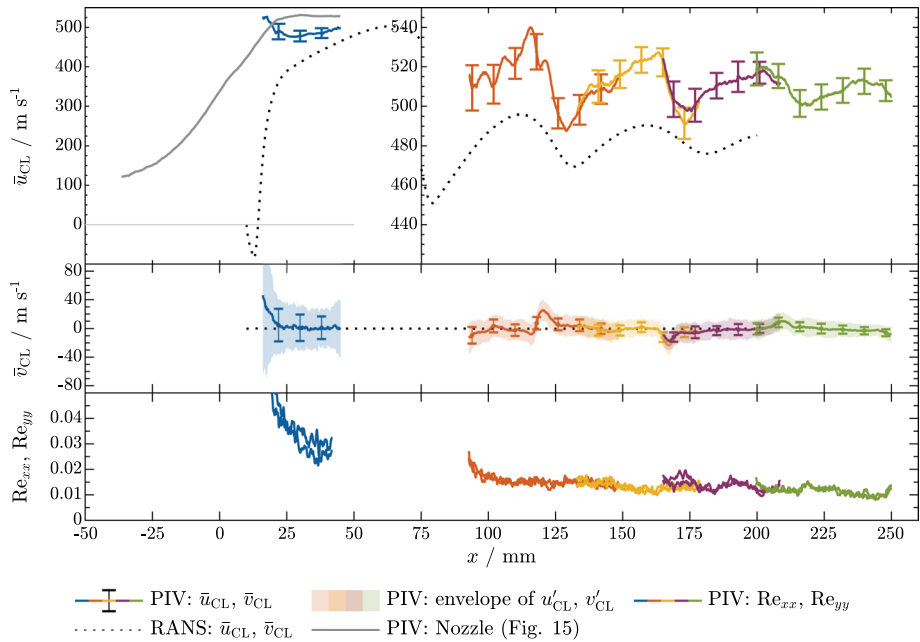


**Fig. 20** *Injector B* wake flow: Measured (PIV) and predicted (RANS) time-averaged velocity components  $\bar{u}_{CL}$ ,  $\bar{v}_{CL}$  and Reynolds stresses  $Re_{xx}$ ,  $Re_{yy}$  along the channel centerline ( $y = z = 0$  mm). The bars refer to the standard deviations  $\sigma_{\bar{u}}$ ,  $\sigma_{\bar{v}}$  originating from turbulent and periodic oscillations of the wake flow. Different colors refer to different (overlapping) measurement positions

downstream of the injector trailing edge. This assessment agrees with the position of the recompression neck at  $x < 20$  mm (see Fig. 12b) and also with previous LIF results (Beuting et al. 2018b), which found that the zone of incomplete mixing extends 16 mm downstream of the point of injection. In addition, the fact that only the main flow was seeded with particles also underpins that, wherever PIV results can be obtained, sufficient mixing between the main and injector flow must have been completed.

The measured  $\bar{u}_{CL}$ -distribution in the second window ( $x > 75$  mm) is shaped by the recompression wave intersections, which cause alternating abrupt deceleration followed by a continuous re-acceleration. Here, the positions of locally minimum  $\bar{u}_{CL}$  mark the positions where the reflected shock waves cross the channel center line. These agree with the shock wave cross sections in the Schlieren image (see Fig. 12b,  $100 \text{ mm} < x < 250 \text{ mm}$ ). Different colors, as in the case of injector A, refer to different measurement positions. Again, the results from different positions overlap and, thus, verify the stationary flow field and repeatable PIV measurements.

In the absence of vortex shedding, error bars of  $\bar{u}_{CL}$  and  $\bar{v}_{CL}$  represent turbulent fluctuations only in the wake of injector B. Nevertheless, the fluctuations are clearly enhanced by the turbulent character of the wake within the nozzle; at the nozzle exit they are of about the same magnitude as in the case of injector A. However, in contrast to the injector A wake, the turbulence level decays further from about 0.02 to 0.01 within the second viewing window.

Figure 20 further reveals that the RANS simulation fails to correctly predict the centerline velocity: The predicted  $\bar{u}_{CL}$  underestimates the PIV measurements by a constant



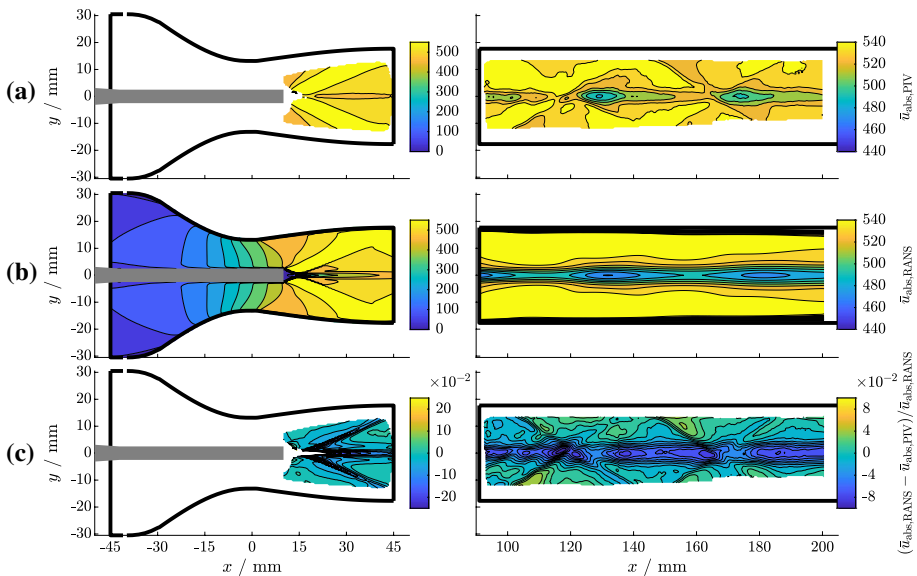
offset of about 20m/s in module 3 ( $x > 75$  mm). The contour plot of the absolute velocity  $\bar{u}_{abs}$  (Fig. 21) shows that the mixing between the main and the injected flow is apparently underestimated. This large deviation results from differences in the vertical mean flow velocity  $\bar{v}$  itself. This is a typical shortcoming of the RANS approach, which is known to suppress most of the unsteady structures of the flow (Luo et al. 2015). As a consequence, the high frequent turbulent structures that strongly enhance the mixing at the shear layer edge are suppressed in the simulation. This shortcoming becomes particularly apparent at the nozzle exit ( $x > 25$  mm), where high Reynolds stresses of comparable magnitude with the case of injector A point to the existence of small-scale turbulent structures.

### 4.4.2 Turbulence Statistics

The turbulent character of the wake is also reflected in the Reynolds stresses  $Re_{xx}$ ,  $Re_{yy}$ . Both are elevated near the injector trailing edge and decay to  $< 2\%$  in the supersonic flow region of module 3. Interestingly,  $Re_{xx}$ ,  $Re_{yy}$  are level in this case. This seems to result from the supersonic wake characteristics that do not favour a direction of disturbances (no periodic shedding).

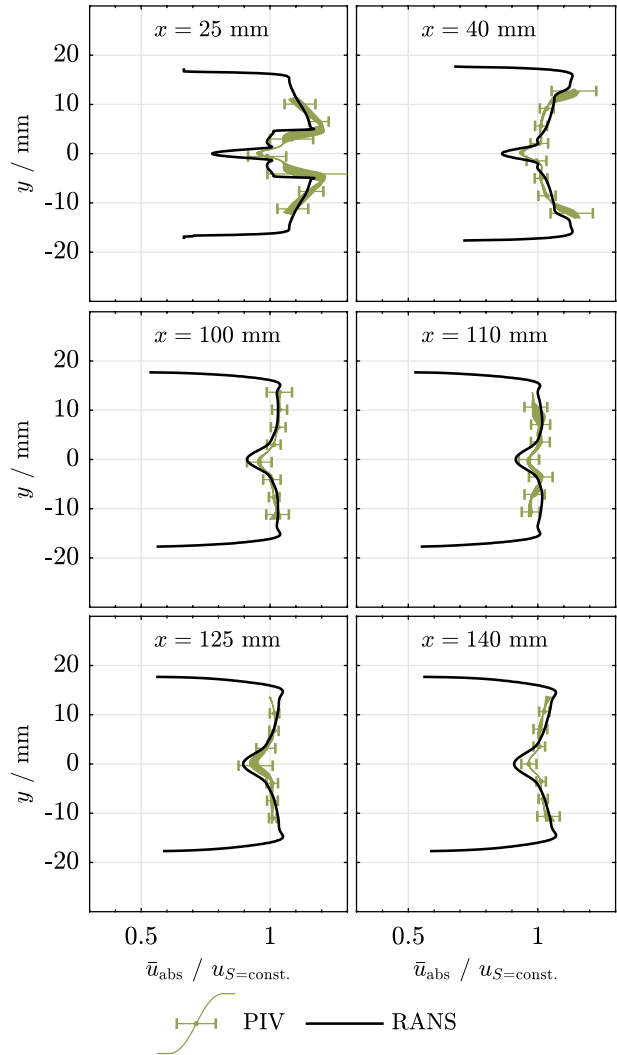
### 4.4.3 Velocity Profiles

Figure 22 depicts velocity profiles at different streamwise positions in the injector B wake. The wake deficit quickly decays as the flow is accelerated within the nozzle but remains, though very small, throughout the test section. Furthermore, as stated earlier, RANS



**Fig. 21** Injector B wake flow: Contour plots of time-averaged absolute velocity  $\bar{u}_{abs}$ : **a** PIV measurements, **b** URANS simulation, and **c**) relative deviation between PIV and URANS. The black frames outline the geometries of the two side windows; the injector trailing edge is sketched in gray

**Fig. 22** *Injector B wake flow:* Profiles of time-averaged velocity  $\bar{u}_{\text{abs}}/u_{S=\text{const.}}$  normalized w.r.t. the isentropic flow velocity (Eq. 7) at different  $x$ -positions within the convergent-divergent nozzle. The bars denote velocity fluctuations due to periodic and turbulent oscillations



simulation overpredicts the wake deficit. However, outside of the wake the velocities profiles coincide, meaning that all simulated values are within the range of turbulent fluctuations visualized as bars.

## 5 Summary and Conclusions

PIV measurements were conducted to experimentally investigate the velocity profiles and turbulent statistics of two different transonic, accelerated wakes generated by central injectors. The investigated injectors differed by the extent of the trailing edge that was either located upstream (injector A) or downstream (injector B) of the throat of a convergent-divergent nozzle. The main difference between the two wake flows is that the (initial) subsonic wake of injector A is characterized by periodic vortex shedding

and an increased turbulence level in the  $y$ -direction, whereas the supersonic wake of injector B is characterized by oblique shock waves and their periodic interaction with the wake. This leads to a very different behavior of the wake: whereas the induced crossflows of the vortex street help to rapidly reduce the wake deficit downstream of injector A, the periodic shock wave/wake interaction downstream of injector B locally narrows the wake, so that the wake deficit persists far downstream.

In addition to the two wake flows, the undisturbed nozzle flow (without injector/wake) was also investigated as a reference case. Furthermore, (U)RANS simulations using the  $k$ - $\omega$ -SST model were performed to identify to what extent this model is able to correctly predict the time-averaged wake flow field. The major conclusions can be summarized as follows:

#### *Undisturbed nozzle flow*

- $Re_{xx}$  and  $Re_{yy}$  strongly decay from about 8% to  $< 2\%$  due to acceleration to supersonic speed.
- Profiles of  $\bar{u}_{abs}$  show that a velocity deficit at the nozzle centerline develops also in the absence of a wake generator.
- RANS simulation is able to accurately predict the velocity field.

#### *Injector A wake flow*

- The strong acceleration attenuates the wake deficit, which only remains for a distance of  $4h_{ITE}$ . At this point the wake centerline velocity catches up with the centerline velocity of the reference case (undisturbed nozzle flow).
- The flow stays non-isentropic also in the wake far field, where  $Re_{yy} > Re_{xx}$ .
- URANS results are able to qualitatively capture the periodic vortex shedding but deviate from the experimental results near the injector trailing edge. Apart from this, the time-averaged velocity field is very well predicted and may be used for, e.g., evaluating the flow conditions and boundary layer growth.

#### *Injector B wake flow*

- The wake deficit decays quickly while the main flow is accelerated but consists downstream of the convergent-divergent nozzle, throughout the investigated supersonic flow region ( $> 380h_{ITE}$ ).
- $\bar{u}_{CL}$  is shaped by the shock wave interactions, which cause alternating deceleration and re-acceleration.
- Conventional RANS approach suppresses most of the mixing of the injectant with the co-flow resulting in an underestimation of the centerline velocity by about 4%. Apart from this, the time-averaged velocity field is very well predicted and may be used for, e.g., evaluating the flow conditions and the positions of the shock waves.

The present results complement the existing data of transonic wake flows by the velocity field and turbulence statistics. Together with previous experimental investigation (Chun 2009; Wohler et al. 2014; Beuting et al. 2018a, b; Richter et al. 2019), which include measurements of wake growth rates, concentration profiles, shedding frequency, Mach number, temperature and the identification of zones of micro/macro mixing, the present results provide valuable validation data for numerical investigations. In the future,

detailed large eddy simulations of the present cases (injector A/B) are planned. These simulations can then provide further insight into the physics of injectors A and B wake flow behavior.

**Supplementary Information** The online version contains supplementary material available at <https://doi.org/10.1007/s10494-022-00339-5>.

**Acknowledgements** Many thanks goes to Aleksandra Stajic who supported the PIV measurements during her summer school at ITLR. The computer resources for this project have been kindly provided by the Steinbuch Centre of Computing (SCC) at the Karlsruhe Institute of Technology (KIT).

**Author Contributions** JR conducted the PIV experiments, processed the data, created the plots and diagrams, and wrote the first draft of the manuscript. BW supervised the research and contributed to the interpretation of the data. CA contributed to the writing of the paper and created Figs. 11 and 12. All authors commented on previous versions of the manuscript and read and approved the final manuscript.

**Funding** Open Access funding enabled and organized by Projekt DEAL. The authors kindly acknowledge the financial support of this work by the German Research Foundation (Deutsche Forschungsgemeinschaft, DFG) through the research project “Experimental and Numerical Mixing Investigations in a Compressible Nozzle Flow” (WE 2549/31-3).

**Data Availability** All processed, time-averaged PIV data are available for download as supplemental material.

**Open Access** This article is licensed under a Creative Commons Attribution 4.0 International License, which permits use, sharing, adaptation, distribution and reproduction in any medium or format, as long as you give appropriate credit to the original author(s) and the source, provide a link to the Creative Commons licence, and indicate if changes were made. The images or other third party material in this article are included in the article’s Creative Commons licence, unless indicated otherwise in a credit line to the material. If material is not included in the article’s Creative Commons licence and your intended use is not permitted by statutory regulation or exceeds the permitted use, you will need to obtain permission directly from the copyright holder. To view a copy of this licence, visit <http://creativecommons.org/licenses/by/4.0/>.

## References

- ANSYS, Inc. ANSYS® CFX, release 19.0 (2019). [www.ansys.com](http://www.ansys.com)
- ANSYS, Inc. ANSYS CFX-solver theory guide, release 19.1 (2019)
- Amatucci, V., Dutton, J., Kuntz, D., Addy, A.: Two-stream, supersonic, wake flowfield behind a thick base. I-General features. *AIAA J* **30**(8), 2039 (1992). <https://doi.org/10.2514/3.11177>
- Barre, S., Quine, C., Dussauge, J.P.: Compressibility effects on the structure of supersonic mixing layers: experimental results. *J. Fluid Mech.* **259**, 47 (1994). <https://doi.org/10.1017/S0022112094000030>
- Beuting, M., Richter, J., Weigand, B., Dreier, T., Schulz, C.: Application of toluene LIF to transonic nozzle flows to identify zones of incomplete molecular mixing. *Opt. Express* **26**(8), 10266 (2018). <https://doi.org/10.1364/OE.26.010266>
- Beuting, M., Richter, J., Weigand, B., Schulz, C.: Experimental Investigation of the Influence of the Pressure Gradient on the Transonic Mixing Behavior in Blunt-Body Wakes using Tracer LIF. in 48<sup>th</sup> AIAA Fluid Dynamics Conference, Atlanta, GA, USA (2018). <https://doi.org/10.2514/6.2018-3543>
- Carscallen, W., Gostelow, J., Mahallati, A.: Some Vortical Phenomena in Flows over Transonic Turbine Nozzle Vanes Having Blunt Trailing Edges. in 20<sup>th</sup> International Society of Air-breathing Engines Conference, Montreal, Canada (2009)
- Carscallen, W.E., Fleige, H.U., Gostelow, J.P.: Transonic Turbine Vane Wake Flows. in Turbo Expo: Power for Land, Sea, and Air (1996). <https://doi.org/10.1115/96-GT-419>
- Charonko, J.J., Vlachos, P.P.: Estimation of uncertainty bounds for individual particle image velocimetry measurements from cross-correlation peak ratio. *Meas. Sci. Technol.* (2013). <https://doi.org/10.1088/0957-0233/24/6/065301>

- Chun, J.: Experimental investigations of injection, mixing, and reaction processes in supersonic flow applications. Phd thesis, Institut für Thermodynamik der Luft- und Raumfahrt, University of Stuttgart (2009)
- Gerrard, J.H.: The mechanics of the formation region of vortices behind bluff bodies. *J. Fluid Mech.* **25**(2), 401 (1966). <https://doi.org/10.1017/S0022112066001721>
- Goldstein, S.: Modern developments in fluid dynamics, Vol. 2 (Clarendon Press) (1950)
- Grzونا, A., Weiss, A., Olivier, H., Gawehn, T., Gülhan, A., Al-Hasan, N., Schnerr, G., Abdali, A., Luong, M., Wiggers, H., Schulz, C., Chun, J., Weigand, B., Winnemöller, T., Schröder, W., Raket, T., Schaber, K., Goertz, V., Nirschl, H., Maisels, A., Leibold, W., Dannehl, M.: Gas-phase synthesis of non-agglomerated nanoparticles by fast gasdynamic heating and cooling. in *Shock Waves* (Springer Berlin Heidelberg, Berlin, Heidelberg) (2009), pp. 857–862
- Ke, J.: RANS and hybrid LES/RANS simulations of flow over a square cylinder. *Adv. Aerodyn.* **1**, 10 (2019). <https://doi.org/10.1186/s42774-019-0012-9>
- Krstić, M.: Chapter 9 - Mixing Control for Jet Flows. in *Combustion Processes in Propulsion* (Butterworth-Heinemann, Burlington, 2006), pp. 87 – 96. <https://doi.org/10.1016/B978-012369394-5/50013-5>
- LaVision. DaVis, release 8 (2011). [www.centaurosoft.com](http://www.centaurosoft.com)
- Liu, X., Thomas, F.O., Nelson, R.C.: An experimental investigation of the planar turbulent wake in constant pressure gradient. *Phys. Fluids* **14**(8), 2817 (2002). <https://doi.org/10.1063/1.1490349>
- Luo, D., Yan, C., Wang, X.: Computational study of supersonic turbulent-separated flows using partially averaged Navier-stokes method. *Acta Astronaut.* **107**, 234 (2015). <https://doi.org/10.1016/j.actastro.2014.11.029>
- Menser, J., Dreier, T., Kaiser, S., Schulz, C.: Multi-pulse RGB illumination and detection for particle tracking velocimetry. in *7<sup>th</sup> European Combustion Meeting*, Budapest, Hungary (2015)
- Menter, F.R.: Two-equation eddy-viscosity turbulence models for engineering applications. *AIAA J.* **32**(8), 1598 (1994). <https://doi.org/10.2514/3.12149>
- Menter, F.R.: Tracer particles and seeding for particle image velocimetry. *Meas. Sci. Technol.* **8**(12), 1406–1416 (1997). <https://doi.org/10.1088/0957-0233/8/12/005>
- Motallebi, F., Norbury, J.F.: The effect of base bleed on vortex shedding and base pressure in compressible flow. *J. Fluid Mech.* **110**, 273 (1981). <https://doi.org/10.1017/S0022112081000748>
- Nakagawa, M., Dahm, W.J.A.: Virtual origin of incompressible and supersonic turbulent bluff-body wakes. *AIAA J.* **43**, 697 (2005). <https://doi.org/10.2514/1.10928>
- Nakagawa, M., Dahm, W.J.A.: Scaling properties and wave interactions in confined supersonic turbulent bluff-body wakes. *AIAA J.* **44**(6), 1299 (2006). <https://doi.org/10.2514/1.19772>
- Narasimha, R., Sreenivasan, K.: Relaminarization of fluid flows. *Adv. Appl. Mech.* **19**, 221 (1979). [https://doi.org/10.1016/S0065-2156\(08\)70311-9](https://doi.org/10.1016/S0065-2156(08)70311-9)
- Papamoschou, D., Roshko, A.: The compressible turbulent shear layer: an experimental study. *J. Fluid Mech.* **197**, 453 (1988). <https://doi.org/10.1017/S0022112088003325>
- Raffel, M., Willert, C. E., Scarano, F.: *Particle Image Velocimetry, A Practical Guide* (Springer International Publishing) (2018)
- Ragni, D., van Oudheusden, B.W., Scarano, F.: Particle tracer response across shocks measured by PIV. *Exp. Fluids* **50**, 53 (2011). <https://doi.org/10.1007/s00348-010-0892-2>
- Richter, J., Beuting, M., Schulz, C., Weigand, B.: Mixing processes in the transonic, accelerated wake of a central injector. *Phys. Fluids* **31**, 016102 (2019). <https://doi.org/10.1063/1.5055749>
- Richter, J., Mayer, J., Weigand, B.: Accuracy of non-resonant laser-induced thermal acoustics (LITA) in a convergent-divergent nozzle flow. *Appl. Phys. B* **124**(2), 19 (2018). <https://doi.org/10.1007/s00340-017-6885-6>
- Richter, J., Beuting, M., Schulz, C., Weigand, B.: Numerical investigation of transonic mixing behavior in the wake of a central injector at different Reynolds numbers. in *48<sup>th</sup> AIAA Fluid Dynamics Conference*, Atlanta, GA, USA (2018). <https://doi.org/10.2514/6.2018-3544>
- Richter, J., Beuting, M., Dreier, T., Schulz, C., Steinhausen, C., Weigand, B.: Non-intrusive frequency measurements of bluff-body vortex shedding at high Reynolds numbers. in *23<sup>rd</sup> International Society of Air-breathing Engines Conference*, Manchester, Great Britain (2017)
- Richter, J., Beuting, M., Schulz, C., Dreier, T., Weigand, B.: Macroscopic Mixing Investigation in a Compressible Accelerated Nozzle Flow using Toluene Tracer LIF. in *18<sup>th</sup> International Symposium on Applications of Laser and Imaging Techniques to Fluid Dynamics*, Lisbon, Portugal (2016)
- Roshko, A.: On the development of turbulent wakes from vortex streets. *Tech. Rep. NACA-TN-2913*, National Advisory Committee for Aeronautics; Washington, DC, United States (1953)
- Roshko, A.: On the drag and shedding frequency of two-dimensional bluff bodies. *Tech. Rep. NACA-TN-3169*, National Advisory Committee for Aeronautics; Washington, DC, United States (1954)

- Samimy, M., Lele, S.K.: Motion of particles with inertia in a compressible free shear layer. *Phys. Fluids A* **3**(8), 1915 (1991). <https://doi.org/10.1063/1.857921>
- Scarano, F., Oudheusden, B.: Planar velocity measurements of a two-dimensional compressible wake. *Exp. Fluids* **34**(3), 430 (2003). <https://doi.org/10.1007/s00348-002-0581-x>
- Smits, A.J., Dussauge, J.P.: Turbulent shear layers in supersonic flow (Springer Science & Business Media) (2006). <https://doi.org/10.1007/b137383>
- Uzol, O., Camci, C.: The effect of sample size, turbulence intensity and the velocity field on the experimental accuracy of ensemble averaged PIV measurements. in 4<sup>th</sup> International Symposium on Particle Image Velocimetry, Göttingen, Germany (2001)
- Winnemöller, T., Meinke, M., Schröder, W.: Turbulent mixing in an accelerated nozzle flow. *Int. J. Heat Fluid Flow* **31**(3), 342 (2010). <https://doi.org/10.1016/j.ijheatfluidflow.2010.02.022>
- Winnemöller, T., Meinke, M., Schröder, W.: Comparison of the mixing efficiency of different injector configurations. *Comput. Fluids* **117**, 262 (2015). <https://doi.org/10.1016/j.compfluid.2015.05.017>
- Wohler, A., Weigand, B., Mohri, K., Schulz, C.: Mixing processes in a compressible accelerated nozzle flow with blunt-body wakes. *AIAA J.* **52**(3), 559 (2014). <https://doi.org/10.2514/1.J052493>
- Wynanski, I., Champagne, F., Marasli, B.: On the large-scale structures in two-dimensional, small-deficit, turbulent wakes. *J. Fluid Mech.* **168**, 31 (1986). <https://doi.org/10.1017/S0022112086000289>
- Yang, X., Tucker, P.G.: Assessment of turbulence model performance: severe acceleration with large integral length scales. *Comput. Fluids* **126**, 181 (2016). <https://doi.org/10.1016/j.compfluid.2015.12.007>